Supporting Information

Hydrothermal synthesis and controlled growth of group-VIB W metal compound nanostructures from tungsten oxide to tungsten disulphide

Xue Wang[1], Cheng-Bao Yao[1, *], Li-Yuan Wang[1], Ze-Miao Wang[1], Cai-Hong Jiang[1] and Xiao-Jie Liu[1, *]

[1]*Key Laboratory of Photonic and electric Bandgap materials, Ministry of Education, School of Physics and Electronic*

Engineering, Harbin Normal University, Harbin, 150025, Heilongjiang Province, China

*Corresponding author：yaochengbao5@163.com, 378599603@qq.com

1. Hydrothermal conditions for sample preparation

(i) WO_3 nanorods.

WO_3 nanorods were prepared at different reactant concentration for different temperatures and varying reaction time, respectively. Reactant concentration was changed while controlling other conditions at 240 °C and 12 h, to obtain the three samples termed as WO_3-C1, WO_3-C2 and WO_3-C3 nanorods, corresponding to the millimolar ratios of C_2H_5NS to WCl_6 is 10 : 2, 15 : 3 and 20 : 4, separately. When millimolar ratios of C_2H_5NS to WCl_6 is 15 : 3, the hydrothermal reactions were carried out at 220 °C, 240 °C and 260 °C for 12 h, respectively. And the samples were marked as WO_3-T1, WO_3-T2 and WO_3-T3 nanorods. Under the reaction conditions at 260 °C and 15 : 3, the reaction time was adjusted to obtain WO_3-t1 (8 h), WO_3-t2 (12 h) and WO_3-t3 (24 h) nanorods. Here, WO_3-T2 is WO_3-C2 and WO_3-T3 is WO_3-t2.

(ii) WS_2 nanosheets.

When millimolar ratios of C_2H_5NS to WCl_6 is 20 : 2, WS_2 nanosheets were prepared at different temperatures for varying reaction time, respectively. WS_2-T1, WS_2-T2, WS_2-T3, WS_2-T4 and WS_2-T5

nanosheets were obtained at 160 °C, 180 °C, 220 °C, 240 °C and 260 °C for 12 h, respectively. WS_2-t1, WS_2-t2 and WS_2-t3 nanosheets were prepareed at 240 °C for 12 h, 18 h and 24 h, respectively. Here, WS_2-t1 is WS_2-T4. At 240 °C, different the millimolar ratios of C_2H_5NS to WCl_6 were used as reactant for a 12 h hydrothermal reaction. $WS_{2(7:1)}$-240°C, $WS_{2(8:1)}$-240°C, $WS_{2(9:1)}$-240°C, $WS_{2(10:1)}$-240°C were obtained.

(iii) WS_xO_y nanocomposites

Cooling treatment. Keeping other hydrothermal conditions consistent with WO_3-C2, the $WSO_{5:1}$-180 °C and $WSO_{5:1}$-160 °C were obtained under 180 °C and 160 °C, respectively.

Adding S source. $WSO_{6:1}$-160 °C was obtained by adding S source on the basis of $WSO_{5:1}$-160 °C.

The Fig. S1 summarizes the types of samples obtained under different hydrothermal conditions. It is clear that the sample composition and structure can be regulated by the reactant ratio ($C_2H_5NS : WCl_6$) and the hydrothermal temperature.
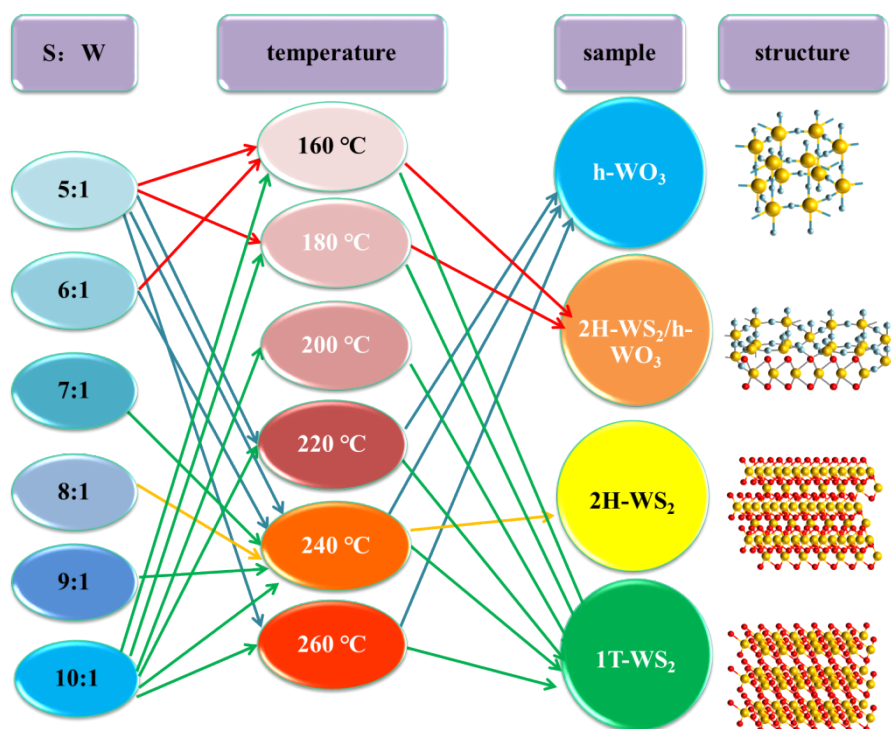

Fig. S1 Summary of experimental conditions.

2. **Different morphologies and compositions under different hydrothermal conditions**

(i) WO_3 nanorods.

The SEM images of WO_3-C1-C3, WO_3-T1-T3 and WO_3-t1-t3 were shown in Fig. S2 (a_i-a_{iii}, b_i-b_{iii} and c_i-c_{iii}). All EDS images (Fig. S2 (a_{iv}-c_{iv})) showed W and O elements, indicating that the samples are composed of tungsten oxide. S mostly existed in the solution in the form of SO_4^{2-}, which assists the formation of 1D h-WO_3 nanorods. The above results showed that 1D WO_3 nanorods are obtained at high temperature (220 °C-240 °C) under S : W = 5 : 1.
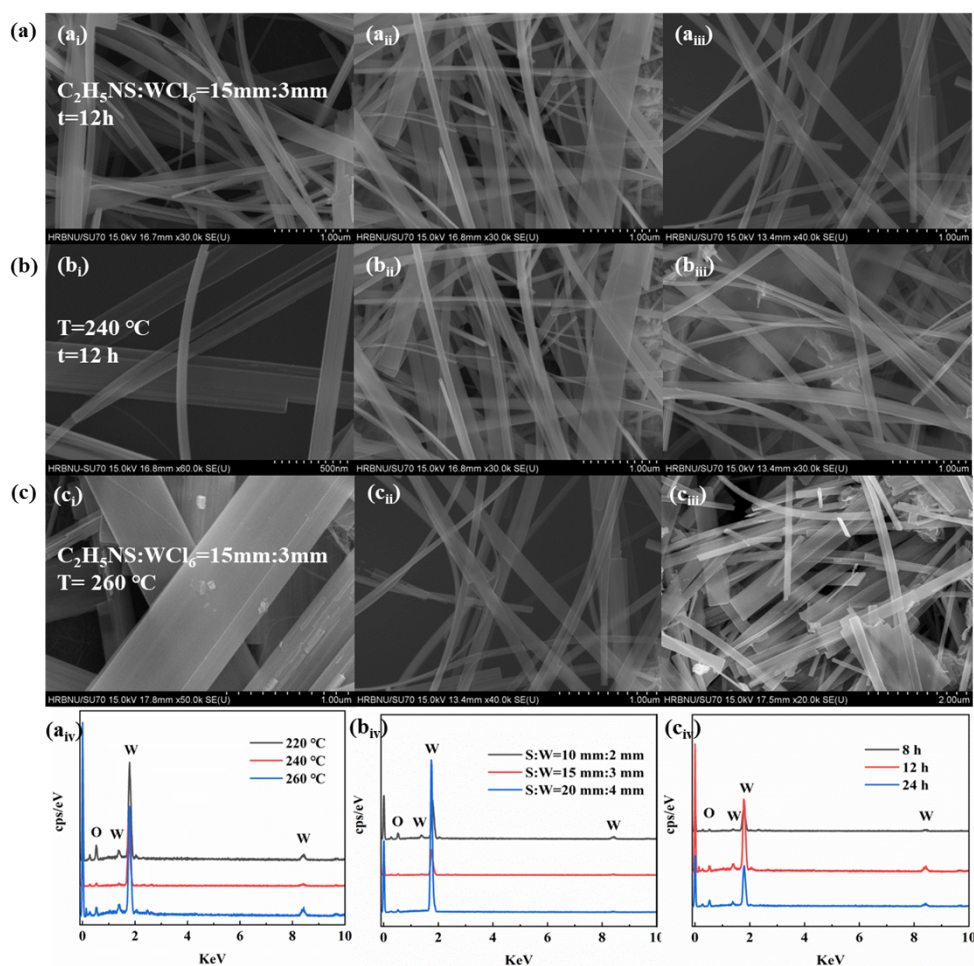

Fig. S2 SEM and EDS images of samples, which hydrothermal reactions at different temperatures (a), reactant concentration (b) and reaction time (c).

(ii) WS_2 nanosheets.

The SEM images of WS$_2$-T1-T5 and WS$_2$-t1-t3 were shown in Fig. S3 (a$_i$-a$_v$ and b$_i$-b$_{iii}$), indicating that the samples were all composed of nanoflowers spontaneously aggregated by nanosheets. All EDS images (Fig. S3 (a$_{vi}$, b$_{iv}$)) shown W and S elements, indicating that the samples were composed of tungsten sulfide. Fig. S3 (c) showed the formation process of WS$_2$ nanoflowers. The short WO$_3$ nanosheets were still formed first during the early stage of the hydrothermal reaction, and were sulfided into dispersed WS$_2$ nanosheets before the WO$_3$ nanorods aggregate into clusters. As the nanosheets gradually grow, WS$_2$ can spontaneously agglomerate to form WS$_2$ nanoflowers on the basis of uniform nanosheets.
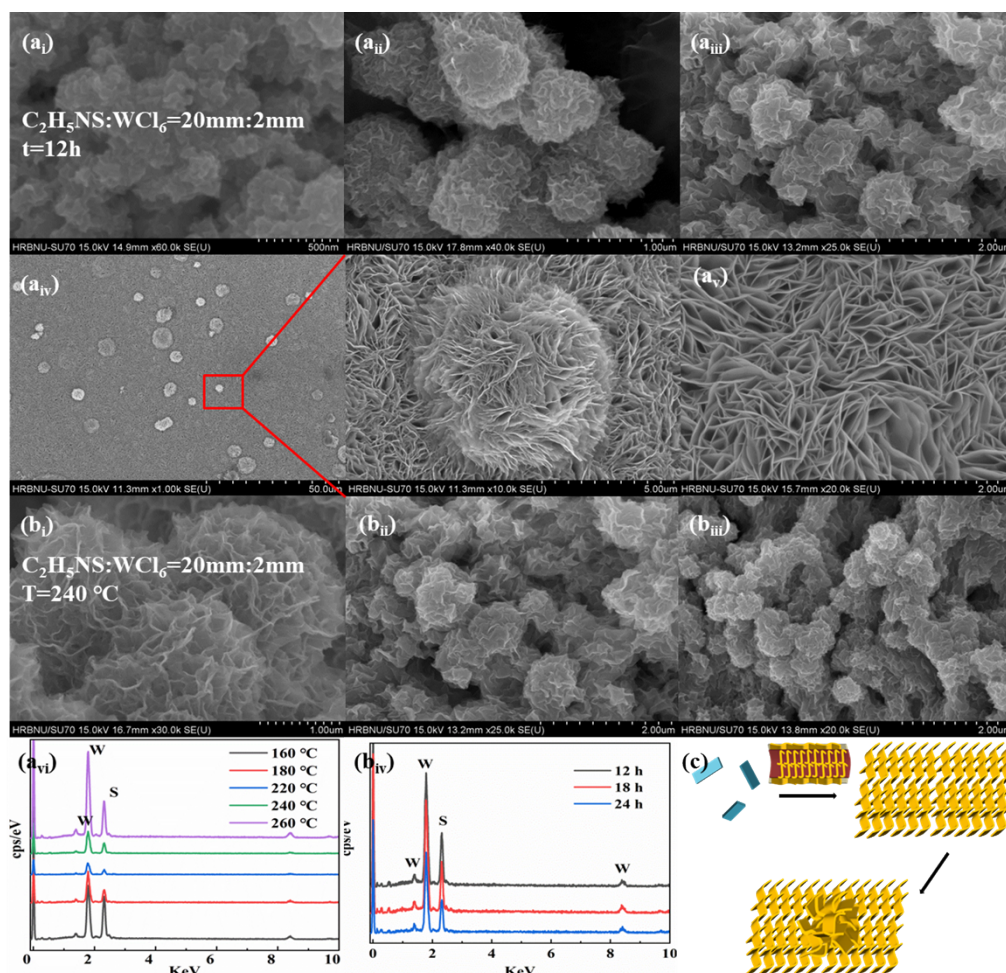

Fig. S3 SEM and EDS images of samples, which hydrothermal reactions at different temperatures (a) and reaction time (b), the formation process of WS$_2$ nanoflowers (c).

(iii) WS$_x$O$_y$ nanocomposites

The SEM images of WS$_x$O$_{y(6:1)}$-160 °C were displayed in Fig. S4 (a). It was obvious that the samples were composed of nanorod clusters (WO$_3$) and nanoflowers (WS$_2$). To explore changes in the elemental composition of the samples, the EDS images were shown in the Fig. S4 (b). The result showed that the sample was composed of S, W, O elements, and the content of S element in the sample was increased compared with WS$_x$O$_{y(5:1)}$-160 °C, indicating that increasing the concentration of S source in the reactant will result in more WO$_3$ being sulfided. In the Fig. S4 (c), WS$_x$O$_{y(6:1)}$-160 °C exhibited the same diffraction peaks as WS$_x$O$_{y(5:1)}$-160 °C, illustrating that WS$_x$O$_{y(6:1)}$-160 °C consisted of h-WO$_3$ and 2H-WS$_2$. The Fig. S4 (d-f) showed a structure of nanosheet-wrapped nanorod cluster. EDS elemental mapping images showed that nanorods were mainly composed of W, O elements and nanosheets were mainly composed of W, S elements (Fig. S4 (e)). The TEM image of a single WO$_3$ nanorod was magnified in Fig. S4 (g). The nanorods were having lattice fringe width of ~0.617 nm corresponding to (100) crystal planes of WO$_3$. The lattice spacing of adjacent nanosheets was observed to be 0.265 nm, which was attributed to the (101) crystal planes of WS$_2$. The lattices of the two were tightly connected, indicating that WO$_3$ acted as a template during the vulcanization process.
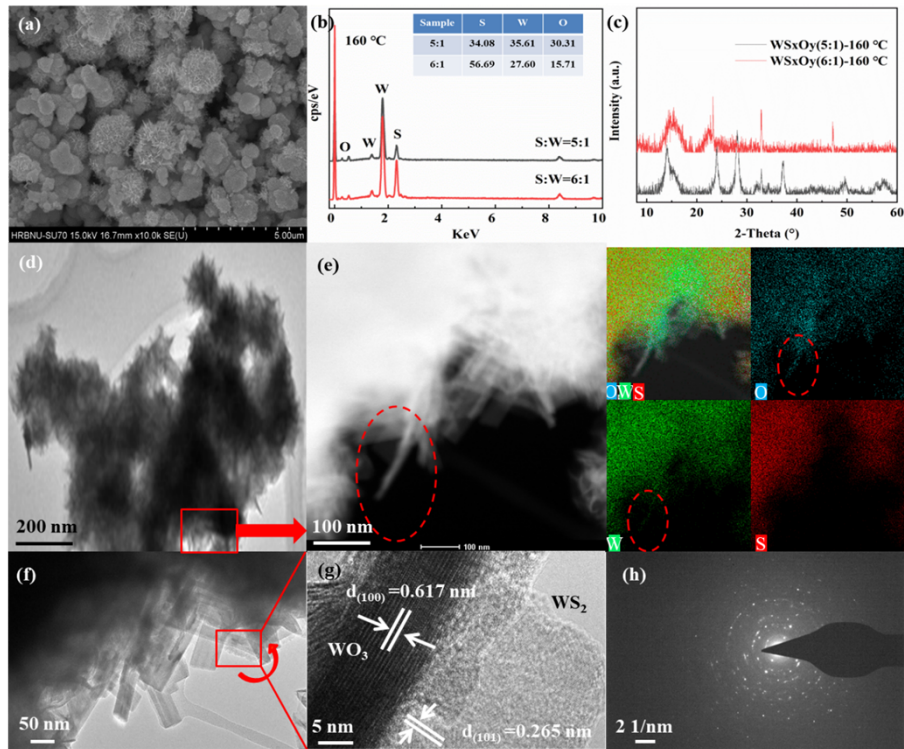
Fig. S4 SEM (a), EDS (b), XRD (c) and TEM (d-h) images of $WS_xO_{y(6:1)}$-160 ℃ .

3. The property analysis.

(i) Raman analysis

In Fig. S5 (a), Raman vibration peak of $WO_{3(5:1)}$-240 °C and $WO_{3(6:1)}$-240 °C located at 96 cm^{-1}, the range of 150-330 cm^{-1} and ~717 cm^{-1}, corresponding to the lattice vibration, the weak bending vibration of δ(O-W-O) and the stretch vibration of v(O-W-O) respectively. In Fig. S5 (b), the two vibrational peak of WS_2 located at ~400 cm^{-1} were sharp, indicating that the vibrational mode of WS_2 was stronger in WS_xO_y. At the same time, the v(O-W-O) peaks of WO_3 were also enhanced, which may be due to the interaction between WS_2 and WO_3. In Fig. S5 (c), the E^1_{2g} and A_{1g} vibration peaks of WS_2 appeared at ~350 and 420 cm^{-1}, revealing that the sample was pure WS_2.

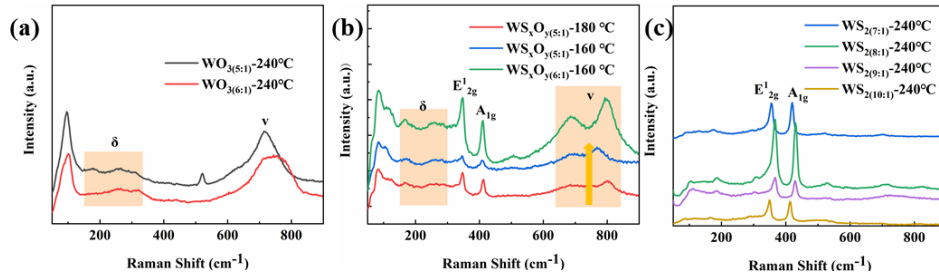Fig. S5 Raman images of (a) WO_3, (b) WS_xO_y and (c) WS_2.

(ii) UV-vis analysis

The UV-vis spectrum of WO_3, WS_xO_y and WS_2 were displayed in Fig. S6 (a-c), respectively. In Fig. S6 (a), the absorption peaks of WO_3 at 220 nm and 280 nm originated from the internal charge transfer of $[WO_6]$ octahedra. An absorption peak of WO_3 appeared at 250 nm, it can be speculated that the peak comes from O_v in WO_3. In Fig. S6 (b), the peak originated from O_v of WO_3 at 250 nm disappeared and the peak located at 260 nm from B excitons of WS_2 was increased with the strengthening of vulcanization. It was clear that the absorption of the WS_xO_y in the visible range was significantly enhanced. In Fig. S6 (c), the 260 nm peak originated from B absorption of WS_2.
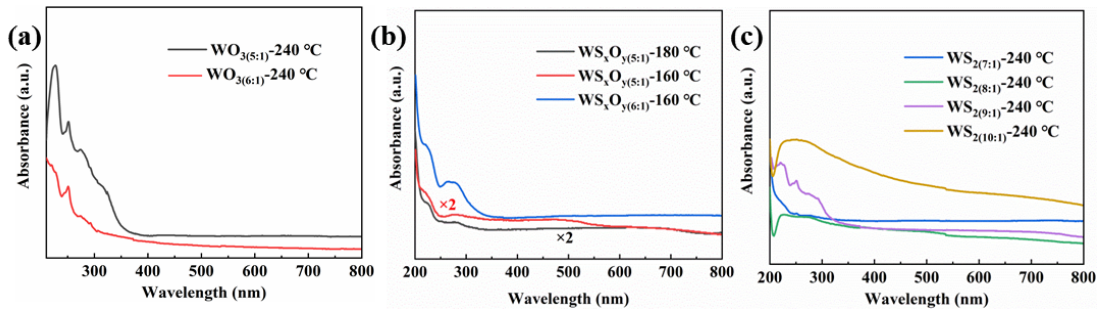

Fig. S6 UV-vis images of WO_3 (a), WS_xO_y (b) and WS_2 (c).

(iii) PL analysis

In Fig. S7 (a), the emission peaks of WO_3 located at 416 nm, 553 nm and 760-820 nm, corresponding to interband transition, defect state and phonons luminescence with indirect transitions. In Fig. S7 (b), luminescence behavior and intensity are regulated by the sulfidation, due to the situation of O_v and S substitution during the sulfidation process. In Fig. S7 (c), the constant energy difference between A and

B is ~0.4 eV, independent of the layer number.

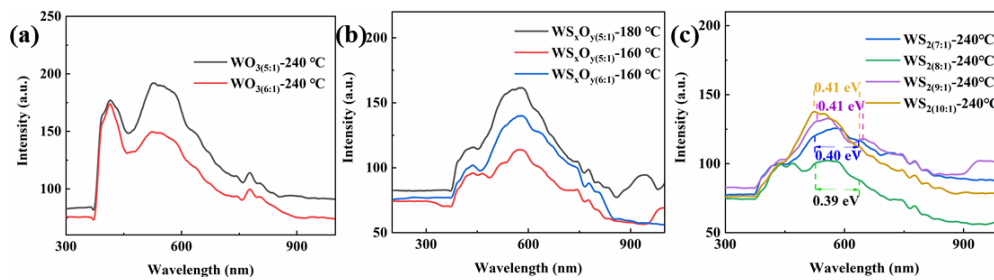Fig. S7 PL images of WO$_3$ (a), WS$_x$O$_y$ (b) and WS$_2$ (c).